



# High-performance PtCu<sub>x</sub>@Pt core-shell nanoparticles decorated with nanoporous Pt surfaces for oxygen reduction reaction



Namgee Jung<sup>a,1</sup>, Yeonsun Sohn<sup>b,1</sup>, Jin Hoo Park<sup>b</sup>, Kee Suk Nahm<sup>b</sup>, Pil Kim<sup>b,\*</sup>,  
Sung Jong Yoo<sup>c,d,\*</sup>

<sup>a</sup> Graduate School of Energy Science and Technology (GEST), Chungnam National University, 99 Daehak-ro, Yuseong-gu, Daejeon 305-764, Republic of Korea

<sup>b</sup> School of Semiconductor and Chemical Engineering, Department of Energy Storage Conversion Engineering, Nanomaterial Process Research Center, Chonbuk National University, Jeonju 561-756, Jeonbuk, Republic of Korea

<sup>c</sup> Fuel Cell Research Center, Korea Institute of Science and Technology (KIST), Seoul 136-791, Republic of Korea

<sup>d</sup> Clean Energy and Chemical Engineering, Korea University of Science and Technology, Daejeon 34113, Republic of Korea

## ARTICLE INFO

### Article history:

Received 2 November 2015

Received in revised form 12 April 2016

Accepted 16 May 2016

Available online 17 May 2016

### Keywords:

Porous nanoparticle

Core-shell

Galvanic replacement

Catalyst

Oxygen reduction reaction

Fuel cell

## ABSTRACT

PtCu<sub>x</sub>@Pt/C ( $x = 3, 5$ , and  $7$ ) core-shell catalysts with nanoporous Pt surfaces were synthesized via the galvanic replacement reaction. The surface morphology and elemental compositions of the PtCu<sub>x</sub>@Pt/C catalysts were significantly influenced by the initial ratio of Cu to Pt in the PtCu<sub>x</sub> nanoparticle substrates, and porous surfaces on the PtCu<sub>x</sub>@Pt nanoparticles could be produced when the Cu to Pt ratios in the PtCu<sub>x</sub> nanoparticle substrates were greater than  $5$ . In addition, the nanoporous PtCu<sub>x</sub>@Pt nanoparticles showed different electronic structures depending on the surface to bulk compositions. Therefore, the oxygen reduction reaction (ORR) activities of the PtCu<sub>x</sub>@Pt/C catalysts were significantly influenced by the surface morphologies and atomic ratios of Cu to Pt near the surface of the nanoparticles. Among the PtCu<sub>x</sub>@Pt/C catalysts synthesized, PtCu<sub>7</sub>@Pt/C catalyst with a nanoporous Pt surface exhibited superior ORR activity and durability compared to a commercially available Pt/C JM catalyst. The  $d$ -band downshift of the PtCu<sub>7</sub>@Pt/C catalyst by the formation of highly porous Pt layers on the Cu-enriched subsurface layer resulted in the enhancement of the catalytic activity and durability for the ORR. High durability of the PtCu<sub>7</sub>@Pt/C catalyst was attributed mainly to the increase in the dissolution potential of the Pt surface layers on the Cu-enriched subsurface layer. The Cu dissolution from the subsurface regions of the nanoparticles was also considerably retarded, owing to the surface protection offered by stable Pt shell layers.

© 2016 Elsevier B.V. All rights reserved.

## 1. Introduction

Multistructured Pt-based catalysts have been extensively developed for achieving improved catalytic activity toward the oxygen reduction reactions (ORRs) at the cathodes of proton exchange membrane fuel cell (PEMFC). Many researchers have studied PtM (where  $M = \text{Co}, \text{Ni}, \text{Fe}$ , and  $\text{Cu}$ ) alloy catalysts, in order to take advantage of the compressive strain and electronic ligand effects imparted by the transition metal atoms [1–4]. In general, Pt-based alloy catalysts show much higher ORR activities than the Pt catalyst. However, the transition metals alloyed with Pt rapidly dissolve in acidic environments during the operation of the PEMFC, which

results in rapid degradation of the catalytic activities of the PtM alloy catalysts [4]. Therefore, the concept of core-shell structures has gained attention, where the dissolution of transition metals is prevented by Pt shell layers [5–8]. In addition, Pt usage can be extremely reduced in such catalysts. Pd, Au, or Ir-based alloy nanoparticles have been predominantly studied as core materials for the core-shell catalysts, but  $3d$  transition metals such as Co, Ni, Fe, and Cu have been rarely considered owing to the difficulties encountered during the synthesis and issues associated with the electrochemical stability of the  $3d$  transition metals.

To circumvent this issue, catalysts with Pt-skin structures have been synthesized by subjecting the PtM alloy catalysts to acid and heat treatments [9–12]. In such catalysts, subsurface transition metal atoms electronically and structurally affect the Pt skin layers, which results in highly active Pt surfaces suitable for catalyzing the ORR. However, the methods for the fabrication of catalysts with Pt-skin structures are highly complicated and a careful han-

\* Corresponding authors.

E-mail addresses: [kimpil1@chonbuk.ac.kr](mailto:kimpil1@chonbuk.ac.kr) (P. Kim), [ysj@kist.re.kr](mailto:ysj@kist.re.kr) (S.J. Yoo).

<sup>1</sup> These authors contributed equally.

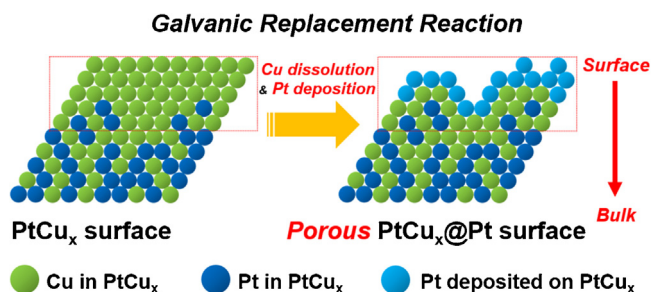
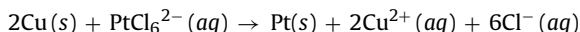


**Fig. 1.** Schematic diagram of the surface morphology of nanoporous  $\text{PtCu}_x\text{@Pt}$  core-shell nanoparticles produced via the galvanic replacement reaction.

ding of materials is required since harsh acidic treatment and high-temperature annealing processes are involved in the synthesis procedures.

Meanwhile, the use of electrochemically dealloyed PtM nanoparticles has been recently investigated for enhancing of the ORR activities of PtM catalysts [13–17]. Electrochemically dealloyed PtM nanoparticles can have Pt-rich surfaces, since the transition metal atoms are intentionally dissolved and the surface Pt atoms are rearranged during potential cycling. In addition, PtM nanoparticles with Pt to M ratios of less than 1 (even lower than 0.3) can be used as starting materials, which is a crucial advantage. Dealloyed PtM nanoparticles with porous surface structures can also be produced when the transition metal content is much higher than the Pt content in the starting PtM alloy nanoparticles. The dealloyed PtM catalysts have been shown to exhibit superior ORR activities compared to the Pt catalyst, owing to their unique surface structure and composition (porous and Pt-rich surfaces). However, in practice, dealloyed PtM catalysts have critical limitations in terms of fabrication, since they can be prepared only on glassy carbon of the rotating disk electrode by electrochemical potential cycling in specific potential ranges (scalability issues). Therefore, it is necessary to develop a facile synthesis method for the mass production of dealloyed nanoparticles with porous and Pt-rich surfaces.

Among the synthesis strategies for dealloyed PtM nanoparticles, the use of galvanic replacement reaction is attractive since the surface structure and composition of the nanomaterials can be easily modified through this process [18–21]. The substrate metal atoms spontaneously dissolve and are replaced by the substituent atoms only when the standard reduction potential of the substrate metal atoms is less positive than that of the substituent metal ion. For example, atoms on a Cu surface can be galvanically replaced with Pt as a result of the difference in the standard reduction potentials between  $\text{PtCl}_6^{2-}/\text{Pt}$  (0.735 V vs. SHE) and  $\text{Cu}^{2+}/\text{Cu}$  (0.337 V vs. SHE) [18], as shown in the following equation.



Furthermore, continuous diffusion of  $\text{PtCl}_6^{2-}$  and  $\text{Cu}^{2+}$  ions during the galvanic replacement reaction can lead to the formation of nanoporous surface structures on the Cu surface when the surface composition of Cu atoms in the alloy nanoparticles and the concentration of Pt ions are systematically controlled [20].

Herein, we propose a facile strategy for the synthesis of carbon-supported nanoporous  $\text{PtCu}_x\text{@Pt}$  core-shell catalysts ( $\text{PtCu}_x\text{@Pt/C}$ ) with a Pt-rich surface and high electrochemical surface area (ESA) via the galvanic replacement reaction for use as catalysts for the ORR, as shown in Fig. 1. Well-alloyed carbon-supported  $\text{PtCu}_x$  nanoparticles ( $\text{PtCu}_x/\text{C}$ ) having various compositions of Pt and Cu were fabricated and used as starting materials. The effect of the ratio of Cu to Pt in the  $\text{PtCu}_x$  nanoparticles on the surface morphologies and ORR activities of the  $\text{PtCu}_x\text{@Pt}$  core-shell catalysts prepared through the galvanic replacement reaction were investigated. In

addition, the durability of the  $\text{PtCu}_x\text{@Pt/C}$  catalysts was evaluated using the accelerated degradation test (ADT) and compared to that of the Pt/C catalyst.

## 2. Experimental

### 2.1. $\text{PtCu}_x/\text{C}$ preparation

To fabricate 20 wt.%  $\text{PtCu}_x/\text{C}$  ( $x = 3, 5$ , and 7) substrate materials, 0.196 M  $\text{H}_2\text{PtCl}_6$  (Sigma-Aldrich) (1.00, 0.75, and 0.60 mL for  $x = 3, 5$ , and 7, respectively) and 0.587 M  $\text{CuCl}_2$  (Sigma-Aldrich) (1.00, 1.24, and 1.40 mL for  $x = 3, 5$ , and 7, respectively) solutions were mixed well with Vulcan carbon (0.3 g) in 150 mL of D.I. water (Millipore) (18.3 M $\Omega$  cm) for 1 h using ultrasonication and vigorous stirring.  $\text{NaBH}_4$  (Sigma-Aldrich) solution was slowly added dropwise to the solution containing the metal precursors and carbon. After reduction for 1 h,  $\text{PtCu}_x/\text{C}$  powders were obtained by filtration with copious amounts of D.I. water and drying in an oven at 60 °C for 12 h. The  $\text{PtCu}_x/\text{C}$  powders were then annealed at 700 °C for 1 h in a  $\text{H}_2$  atmosphere in a furnace.

### 2.2. $\text{PtCu}_x\text{@Pt/C}$ preparation

To deposit Pt shell layers on the  $\text{PtCu}_x$  nanoparticle surfaces, the galvanic replacement reaction was conducted to replace Cu with  $\text{Pt}^{4+}$  ions. Annealed  $\text{PtCu}_3/\text{C}$ ,  $\text{PtCu}_5/\text{C}$ , and  $\text{PtCu}_7/\text{C}$  powders were well-dispersed in D.I. water for 1 h using ultrasonication and vigorous stirring.  $\text{H}_2\text{PtCl}_6$  (0.196 M, 0.29 mL) solution was then added dropwise into the solutions containing  $\text{PtCu}_x/\text{C}$ , while  $\text{H}_2$  gas was simultaneously purged through the solutions. After allowing the galvanic replacement reaction to occur for 2 h,  $\text{PtCu}_x\text{@Pt/C}$  catalysts were obtained by filtration using copious amounts of D.I. water and drying in an oven at 60 °C for 12 h.

### 2.3. Electrochemical characterization

Catalyst ink was prepared by mixing the prepared  $\text{PtCu}_x\text{@Pt/C}$  catalysts, Nafion ionomer (Sigma-Aldrich), and isopropyl alcohol (IPA) (99.99%, SK Chemical). A drop (3  $\mu\text{L}$ ) of the catalyst ink was then loaded on a GC (geometric area = 0.196 cm<sup>2</sup>) of a RDE and the electrode was dried in an oven at 60 °C to remove the solvent from the catalyst surface. The metal loadings on the RDE were  $\sim 30 \mu\text{g cm}^{-2}$ . The electrochemical measurements were performed using a three-compartment electrochemical cell with the GC electrode on the RDE, a Pt wire, and saturated calomel electrode (SCE) as the working, counter, and reference electrodes, respectively. All the potential values are presented against the reversible hydrogen electrode (RHE). Cyclic voltammograms (CVs) of the catalysts were measured with a scan rate of 20 mV s<sup>−1</sup> in the potential range of 0.05–1.05 V<sub>RHE</sub> in Ar-saturated 0.1 M  $\text{HClO}_4$  (70%, Sigma-Aldrich). Ar gas (99.999%) flowed continuously into the electrochemical cell during the CV measurements. The ESAs of the catalysts were calculated using the charge density for hydrogen desorption in the  $\text{H}_{\text{upd}}$  region of the CVs. For the ORR tests, the potential was scanned from 0.05 to 1.05 V<sub>RHE</sub> at a rate of 5 mV s<sup>−1</sup> and a RDE rotation speed of 1600 rpm in  $\text{O}_2$ -saturated 0.1 M  $\text{HClO}_4$ .  $\text{O}_2$  gas ( $\geq 99.5\%$ ) continuously flowed into the electrochemical cell during the ORR tests. CVs and ORR polarization curves of commercially available Pt/C JM catalyst were also measured under the same conditions and compared with the  $\text{PtCu}_x\text{@Pt/C}$  catalysts prepared in this study. To compare the electrochemical durabilities of the  $\text{PtCu}_7\text{@Pt/C}$  and Pt/C JM catalysts, they were subjected to the ADT, where the potential was cycled 5000 times between 0.6 and 1.0 V<sub>RHE</sub> at a scan rate of 100 mV s<sup>−1</sup> in  $\text{O}_2$ -saturated 0.1 M  $\text{HClO}_4$ . After the ADT, the CVs

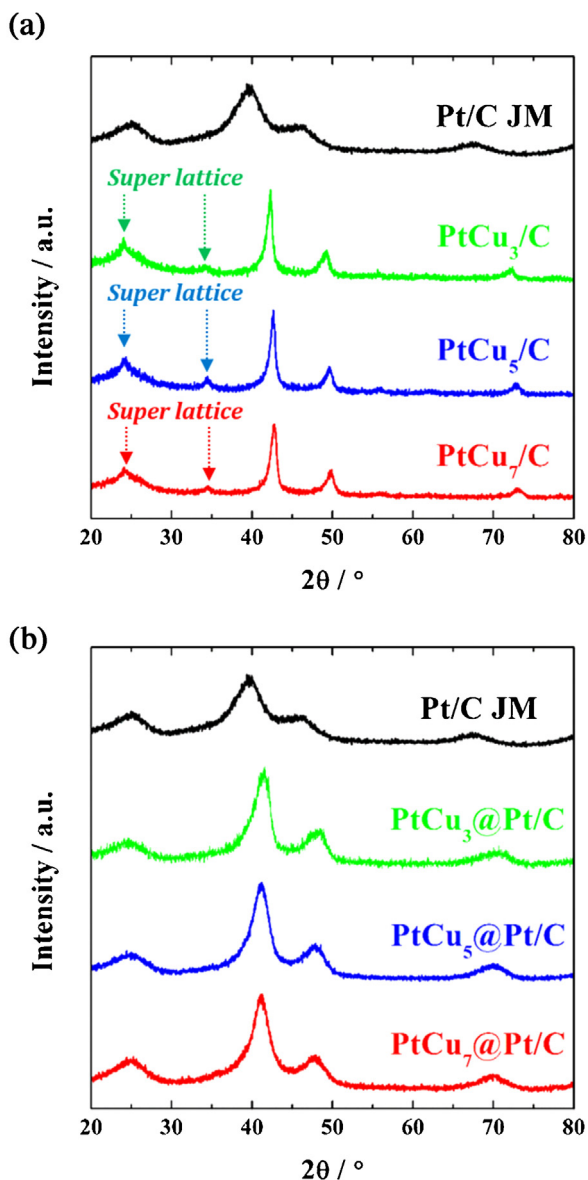


**Fig. 2.** XRD patterns of (a)  $\text{PtCu}_x/\text{C}$  and (b)  $\text{PtCu}_x@\text{Pt}/\text{C}$  samples. XRD pattern of the  $\text{Pt}/\text{C}$  JM as a reference was compared to those of  $\text{PtCu}_x/\text{C}$  and  $\text{PtCu}_x@\text{Pt}/\text{C}$  samples in each figure.

and ORR polarization curves of the catalysts were measured again to detect any changes in the electrochemical properties of catalysts.

#### 2.4. Physical characterization

Using X-ray diffraction (XRD) (Rigaku, D/MAX 2500) with  $\text{Cu K}\alpha$  radiation (40 kV, 200 mA), the diffraction patterns of  $\text{Pt}/\text{C}$  JM,  $\text{PtCu}_x/\text{C}$ , and  $\text{PtCu}_x@\text{Pt}/\text{C}$  catalysts were obtained in the  $2\theta$  range of  $20^\circ$ – $80^\circ$ . Inductively coupled plasma-optical emission spectroscopy (ICP-OES) (Thermo iCAP 6300 series) was performed to determine the bulk compositions of the prepared  $\text{PtCu}_x/\text{C}$  and  $\text{PtCu}_x@\text{Pt}/\text{C}$  catalysts. Further, X-ray photoelectron spectroscopy (XPS) of 8A1 beamline at the Pohang Accelerator Lab (PAL, Pohang, Korea) was used to determine the Cu to Pt ratios on the surface of the  $\text{PtCu}_x@\text{Pt}$  nanoparticles and to analyze the valence bands of the  $\text{PtCu}_x@\text{Pt}/\text{C}$  catalysts. The binding energies were calibrated with respect to the C 1s XPS peak and the experimental data were curve-fitted using the XPSPEAK4.1 software. Morphologies of  $\text{PtCu}_x/\text{C}$ ,  $\text{PtCu}_x@\text{Pt}/\text{C}$ , and  $\text{Pt}/\text{C}$  JM catalyst particles were examined

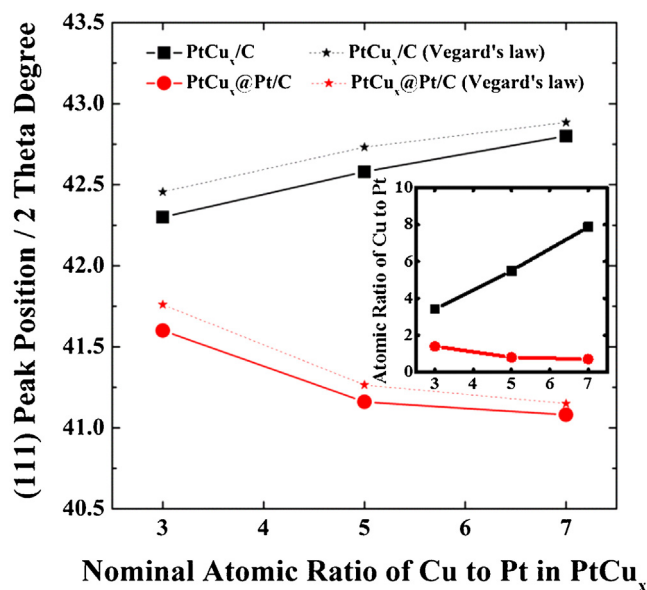


**Fig. 3.** XRD (111) peak positions of  $\text{PtCu}_x/\text{C}$  and  $\text{PtCu}_x@\text{Pt}/\text{C}$ , as a function of the nominal Cu to Pt ratio in  $\text{PtCu}_x$  for  $\text{PtCu}_x/\text{C}$  and  $\text{PtCu}_x@\text{Pt}/\text{C}$ . The dotted lines represent the  $2\theta$  values theoretically calculated using Vegard's law, based on the Cu/Pt ratios in the materials obtained from the ICP-OES results, as shown in the inset.

using high resolution-transmission electron microscopy (HR-TEM) or field emission-transmission electron microscopy (FE-TEM). The compositional changes in the  $\text{PtCu}_7/\text{Pt}/\text{C}$  catalysts before and after the ADT were analyzed by energy-dispersive X-ray spectroscopy (EDX) using the scanning transmission electron microscopy (STEM) capability of FE-TEM.

### 3. Results and discussion

As-prepared  $\text{PtCu}_x/\text{C}$  ( $x=3, 5$ , and  $7$ ) samples may have Cu-rich surfaces due to the difference between standard reduction potentials of Cu and Pt metal ions and the higher concentration of Cu than that of Pt [22]. In addition, during the high-temperature annealing process, the ordered Cu-enriched surfaces were expected to be formed through bulk alloying and surface segregation by the lower surface energy of Cu than that of Pt [23]. Crucially, as shown in Fig. S1 in the Supplementary information, the Cu oxidation ( $\text{Cu}^{2+}/\text{Cu}$ ) peaks were clearly identified between 0.3 and 0.5  $V_{\text{RHE}}$  in the 1st scan CVs of the annealed  $\text{PtCu}_x/\text{C}$  samples [24,25], and the peak areas were significantly increased as the ratios of Cu to Pt were increased. The anodic peak around 0.3–0.5  $V_{\text{RHE}}$  is attributed to the dissolution of low-coordinated Cu surface atoms which are largely surrounded by Cu atoms (bulk-like structure) [25,26]. This is a critical evidence of Cu-enriched surface formation in  $\text{PtCu}_x$  alloy samples.

From the XRD patterns of the annealed  $\text{PtCu}_x/\text{C}$  samples (Fig. 2a), it was confirmed that the prepared  $\text{PtCu}_x$  nanoparticles were suitable for use as core templates. Pt and Cu in the  $\text{PtCu}_x$  nanoparticles were well-alloyed and Cu oxide phases were absent, as a result of the high-temperature annealing process in a  $\text{H}_2$  atmosphere. The XRD patterns of all the  $\text{PtCu}_x$  alloy samples showed (100) and (110) super lattice peaks at  $2\theta$  values of around  $24^\circ$  and  $34^\circ$ , respectively, indicating the presence of well-ordered and intermetallic phases in the  $\text{PtCu}_x$  nanoparticles [27]. In addition, the XRD peak positions were found to be positively shifted as the ratio of Cu to Pt in the  $\text{PtCu}_x$  nanoparticles increased, owing to lattice contractions.

However, after the completion of the galvanic replacement reaction that yield porous  $\text{PtCu}_x@\text{Pt}$  catalysts, the XRD peak positions of  $\text{PtCu}_x@\text{Pt}$  were significantly different from those of the

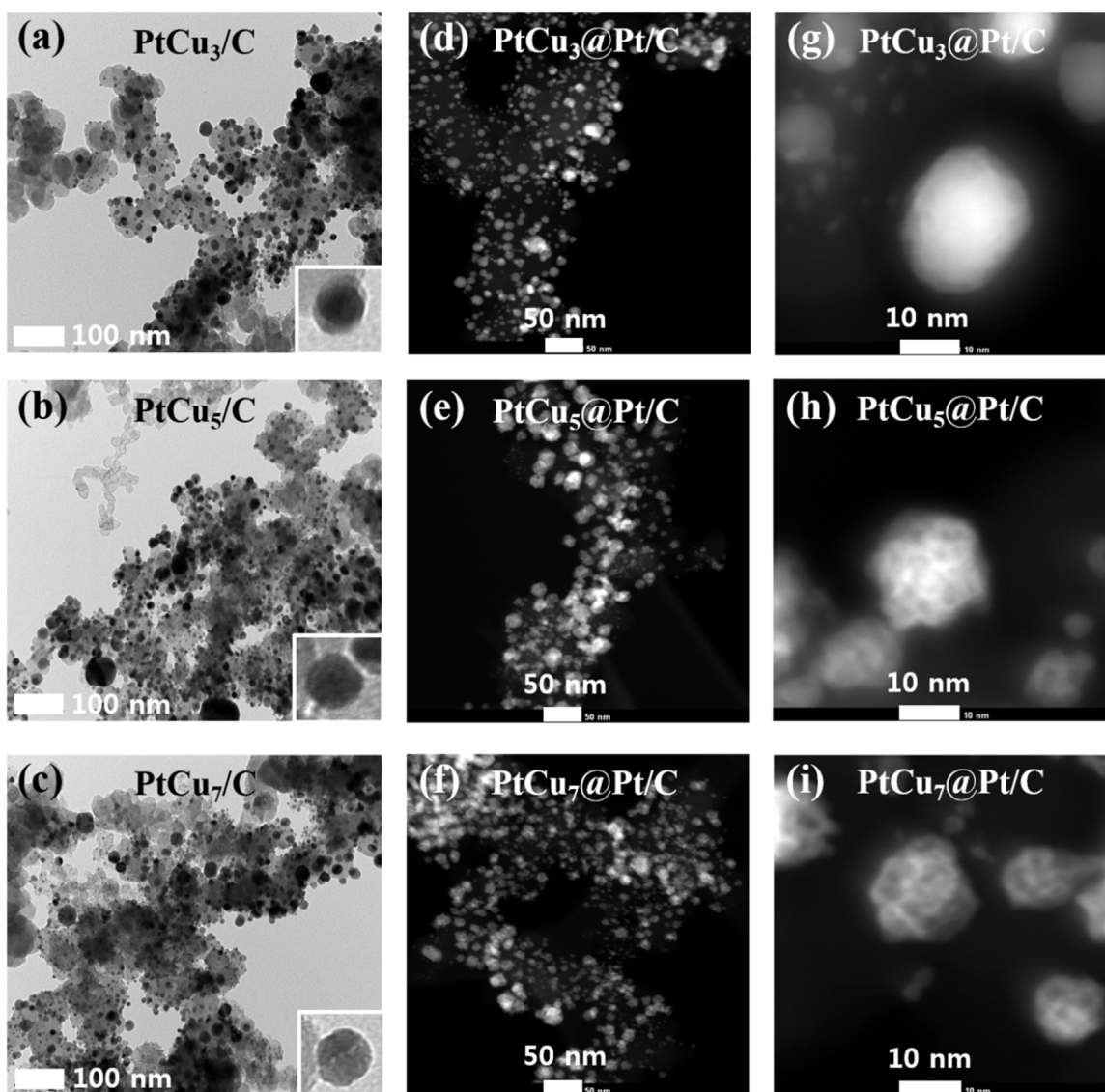


**Fig. 4.** TEM images of (a) PtCu<sub>3</sub>/C, (b) PtCu<sub>5</sub>/C, and (c) PtCu<sub>7</sub>/C samples as starting materials. The insets are the individual particle images enlarged from each TEM image. (d–f) STEM images of PtCu<sub>x</sub>@Pt/C catalysts fabricated from PtCu<sub>x</sub>/C with different ratios of Cu to Pt. (g–i) STEM images of PtCu<sub>x</sub>@Pt/C catalysts with a high magnification.

PtCu<sub>x</sub> nanoparticles as shown in Fig. 2b. The (111) peaks of the PtCu<sub>x</sub>@Pt catalysts were more negatively shifted as the nominal *x* values of PtCu<sub>x</sub> increased. In addition, the super lattice peaks of the ordered intermetallic structures at around 24° and 34° were almost invisible in the case of the PtCu<sub>x</sub>@Pt catalysts, indicating that the galvanic replacement reaction resulted in the formation of dealloyed PtCu<sub>x</sub>@Pt nanoparticles [27].

As shown in Fig. 3, the peak shifts seen in the PtCu<sub>x</sub>@Pt catalysts depended on the final atomic composition (as determined by ICP-OES) of PtCu<sub>x</sub>@Pt, after the core-shell catalysts were fabricated. The Cu to Pt ratios in all the PtCu<sub>x</sub>@Pt catalysts were lower than 2, as shown in the inset of Fig. 3, which may be attributed to the dissolution of Cu and deposition of Pt during the galvanic replacement reactions. However, PtCu<sub>5</sub>@Pt and PtCu<sub>7</sub>@Pt nanoparticles had much lower Cu contents compared to PtCu<sub>3</sub>@Pt nanoparticle. As a result, an increase in the Cu content in the PtCu<sub>x</sub> nanoparticle substrate materials caused an increase in the extent of galvanic replacement of Cu with Pt<sup>4+</sup>. Therefore, PtCu<sub>5</sub>@Pt and PtCu<sub>7</sub>@Pt nanoparticles are expected to have more porous surface structures compared to the PtCu<sub>3</sub>@Pt nanoparticles.

In order to clearly examine the surface morphologies of the PtCu<sub>x</sub>@Pt catalysts, we investigated the particle structures using TEM. As shown in Fig. 4, after the Pt shell layers were formed on the PtCu<sub>x</sub> nanoparticles via the galvanic replacement reaction, the surfaces of the PtCu<sub>5</sub>@Pt and PtCu<sub>7</sub>@Pt nanoparticles became more porous compared to the PtCu<sub>5</sub> and PtCu<sub>7</sub> substrate nanoparticles, respectively. In general, during a galvanic exchange reaction, the oxidation of Cu<sup>0</sup>(s) into Cu<sup>2+</sup>(aq) ions leads to its leaching from the nanoparticle surface and the formation of a pinhole on the surface [28,29]. In addition, the nucleation and deposition of Pt atoms can be occurred simultaneously at various surface sites due to the diffusion of electrons and metal ions on the nanoparticle surface. The continuous diffusion of metal ions (e.g., PtCl<sub>6</sub><sup>2-</sup>) as well as Cu<sup>2+</sup> ion during the reaction would eventually lead to inherited nanopores on the sacrificial Cu surface [28]. As shown in Fig. 4h and i, extremely small pores are clearly identified on PtCu<sub>5</sub>@Pt and PtCu<sub>7</sub>@Pt nanoparticles although they have a broad pore size distribution from several angstrom (Å) to 3–4 nanometer (nm) in diameter.

However, as expected from the XRD and ICP-OES data, the surface structure of the PtCu<sub>3</sub>@Pt nanoparticles was not signifi-

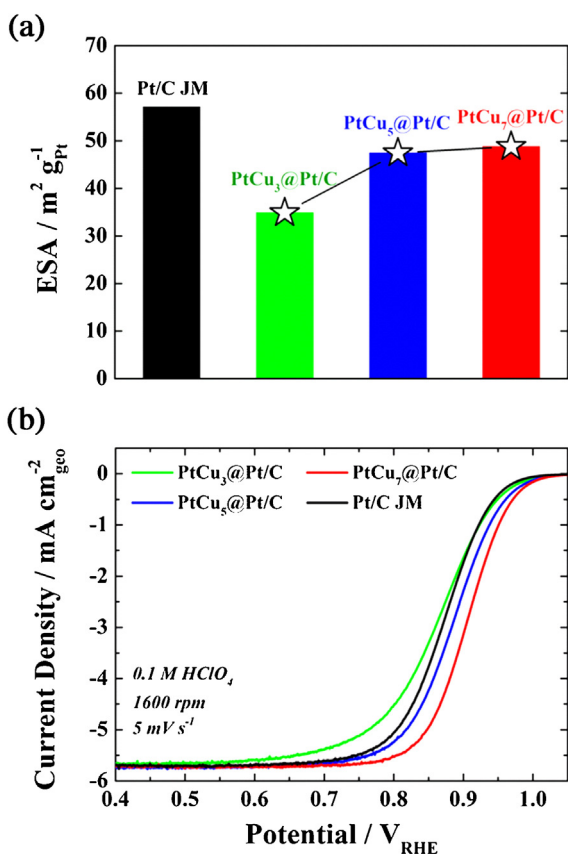


Fig. 5. (a) ESAs and (b) ORR polarization curves of PtCu<sub>x</sub>@Pt/C and Pt/C JM catalysts.

cantly different from the PtCu<sub>3</sub> substrate nanoparticles. In addition, the surface of the PtCu<sub>3</sub>@Pt nanoparticles was relatively smooth compared to those of the PtCu<sub>5</sub>@Pt and PtCu<sub>7</sub>@Pt nanoparticles. Although the particle size of the PtCu<sub>x</sub> and PtCu<sub>x</sub>@Pt nanoparticles varied from less than 5 nm to more than 10 nm as a result of the high-temperature annealing process, the different surface morphologies could be easily identified from the TEM images.

Based on the observation, the interior Cu atoms near the surfaces of the PtCu<sub>5</sub> and PtCu<sub>7</sub> nanoparticles as well as the surface Cu atoms were believed to have dissolved during the galvanic replacement reactions, since the Cu content was rich near the nanoparticle surfaces, whereas in the case of PtCu<sub>3</sub> nanoparticles, only the surface Cu atoms is likely to have participated in the galvanic replacement reaction.

To investigate the effects of the surface structures of the PtCu<sub>x</sub>@Pt catalysts on their electrochemical properties, CVs and ORR polarization measurements were conducted. As shown in Fig. 5a (Fig. S2 in the Supplementary information), although all the PtCu<sub>x</sub>@Pt nanoparticles showed lower ESAs compared to the Pt/C JM catalyst owing to their large particle sizes, it was clear that the ESAs of the PtCu<sub>x</sub>@Pt catalysts increased with an increase in the nominal *x* values of PtCu<sub>x</sub> (i.e. PtCu<sub>3</sub>@Pt/C < PtCu<sub>5</sub>@Pt/C < PtCu<sub>7</sub>@Pt/C). The PtCu<sub>3</sub>@Pt nanoparticle exhibited the smallest ESA among all the porous PtCu<sub>x</sub>@Pt nanoparticles, owing to its smooth Pt surface, as shown in Fig. 4g. However, the ESA of the PtCu<sub>5</sub>@Pt/C catalyst was comparable to that of the PtCu<sub>7</sub>@Pt/C catalyst, since they had similar porous surface morphologies, which was confirmed by the TEM analysis. As shown in Fig. 5b, the ORR activity of the PtCu<sub>3</sub>@Pt/C was the lowest among the PtCu<sub>x</sub>@Pt/C and Pt/C JM catalysts, which might be attributed to its small ESA. On the other hand, the ORR activity of the PtCu<sub>7</sub>@Pt/C catalyst was significantly higher than that

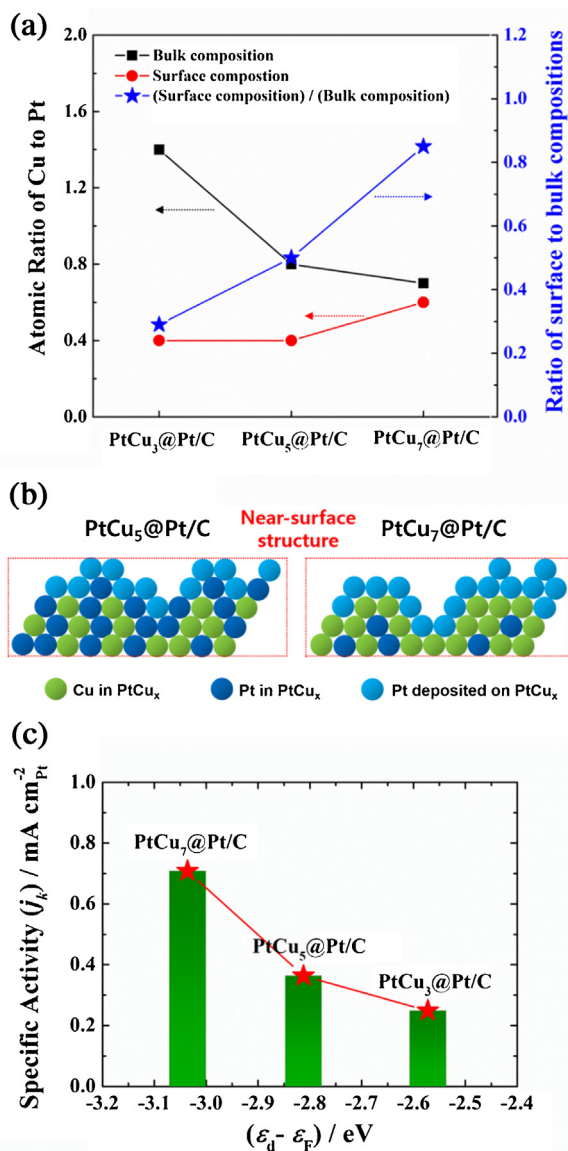


Fig. 6. (a) Atomic ratios of Cu to Pt in the bulk (obtained from ICP-OES) and surface (measured by XPS) and the ratios of surface to bulk Cu/Pt ratios in PtCu<sub>x</sub>@Pt/C catalysts. (b) Schematic diagram of the near-surface structures of PtCu<sub>5</sub>@Pt/C and PtCu<sub>7</sub>@Pt/C catalysts. (c) Specific activities (*j<sub>k</sub>*) of PtCu<sub>x</sub>@Pt/C catalysts at 0.9 V<sub>RHE</sub> as a function of the *d*-band center positions.

of the PtCu<sub>5</sub>@Pt/C catalyst, although they exhibited similar ESA values. Therefore, the different ORR activities of PtCu<sub>5</sub>@Pt/C and PtCu<sub>7</sub>@Pt/C could not be explained by comparing their ESAs alone.

To understand the reasons for the different activities exhibited by the PtCu<sub>x</sub>@Pt/C catalysts towards the ORR, the correlation between the bulk and surface compositions of the PtCu<sub>x</sub>@Pt/C catalysts were carefully examined. We could estimate the surface compositions in the samples from the elemental analysis using XPS (Fig. S3 in the Supplementary information). As shown in Fig. 6a, the Cu to Pt ratios in the bulk decreased as the nominal *x* values in the PtCu<sub>x</sub>@Pt/C catalysts increased, since more Cu atoms were replaced in the PtCu<sub>x</sub> alloy nanoparticles having higher Cu to Pt ratios. In sharp contrast, the Cu to Pt ratios on the surface increased with an increase in the nominal *x* values. As a result, the ratio of the surface to bulk ratio of Cu/Pt in PtCu<sub>7</sub>@Pt/C (0.84) was much higher than the corresponding values in the PtCu<sub>3</sub>@Pt/C (0.29) and PtCu<sub>5</sub>@Pt/C (0.50) catalysts, implying that the PtCu<sub>3</sub>@Pt and PtCu<sub>5</sub>@Pt nanoparticles had higher Cu/Pt ratios in the bulk phases

compared to the surfaces. On the other hand, the Cu/Pt ratio on the surface of PtCu<sub>7</sub>@Pt was comparable to that in the bulk phase. This suggests that in the case of the PtCu<sub>7</sub>@Pt/C catalyst, although many surface Cu atoms are substituted with Pt atoms via the galvanic replacement reaction, a number of near-surface Cu atoms may still remain on the nanoparticle surface.

From the structural point of view, PtCu<sub>7</sub> nanoparticle as a starting substrate material can have plenty of Cu atoms that are not in the vicinity of the Pt atoms particularly near the nanoparticle surfaces. In other words, most of the Pt atoms may serve as a solute near the surface in the alloy nanoparticle. With a decrease in the Cu content in the PtCu<sub>x</sub> nanoparticles, most of the Cu atoms may form a solid lattice structure along with the Pt atoms in the interior of the nanoparticles during PtCu<sub>x</sub> alloy formation. Among the PtCu<sub>x</sub> substrate materials, the number of Cu atoms existing near the nanoparticle surfaces alone without Pt atoms might be the highest in the case of PtCu<sub>7</sub> nanoparticles. As a result, it was concluded that the PtCu<sub>7</sub>@Pt nanoparticles had an abundance of new Pt layers directly contacting subsurface Cu atoms, whereas PtCu<sub>5</sub>@Pt (or PtCu<sub>3</sub>@Pt) nanoparticles had a relatively smaller amount of new Pt layers formed on Cu atoms compared to the amount of new Pt layers deposited on Pt atoms, as shown in Fig. 6b.

In general, when a new Pt layer is formed on the subsurface Cu atoms, the Pt *d*-band structure is downshifted owing to the strain and electronic effects, which results in an increase in the ORR activity of Pt [30–32]. On the other hand, the strain and electronic effects are considerably reduced if the Pt layer is deposited on the subsurface Pt atoms. In this context, the measurement of valence band structures of the catalysts using XPS allowed us to better understand the enhancement in the ORR activity in the PtCu<sub>7</sub>@Pt/C catalyst (Fig. S4 in the Supplementary information). As shown in Fig. 6c, by calculating the *d*-band centers of the PtCu<sub>x</sub>@Pt/C catalysts from the valence band spectra, it was confirmed that the *d*-band centers of PtCu<sub>x</sub>@Pt/C catalysts were downshifted in the order of increasing nominal *x* values (i.e., the *d*-band centers of PtCu<sub>3</sub>@Pt/C > PtCu<sub>5</sub>@Pt/C > PtCu<sub>7</sub>@Pt/C). As a result, PtCu<sub>7</sub>@Pt/C showed an even lower *d*-band center than PtCu<sub>5</sub>@Pt/C, although their surface morphologies and ESAs were similar. Therefore, the PtCu<sub>7</sub>@Pt/C catalyst exhibited enhanced specific activities towards the ORR, owing to the lower *d*-band center compared to the PtCu<sub>5</sub>@Pt/C catalyst, implying that the surface composition as well as the surface morphology and ESA was a decisive factor in determining the ORR activities of PtCu<sub>x</sub>@Pt/C catalysts.

In order to investigate the electrochemical durability of PtCu<sub>7</sub>@Pt/C, which was chosen as a representative porous core-shell catalyst, its CV and ORR polarization curves acquired before and after the ADT were compared with those of the Pt/C JM catalyst. As shown in Fig. 7a and Fig. S5 of the Supplementary information, the change in the ESA of the PtCu<sub>7</sub>@Pt/C catalyst was insignificant (decreased only by ~6.5%) after the ADT, whereas a ~58.0% reduction in ESA was seen in the case of the Pt/C JM catalyst. Furthermore, the ORR activity of the PtCu<sub>7</sub>@Pt/C catalyst was consistent before and after the ADT, as shown in Fig. 7b. On the other hand, the Pt/C JM catalyst showed a severely degraded ORR activity after the ADT, as expected from the CV data.

In order to confirm the structural changes of the PtCu<sub>7</sub>@Pt/C and Pt/C JM catalysts after the ADT, additional TEM analysis was conducted. As shown in Fig. 8a and b, the Cu content in PtCu<sub>7</sub>@Pt/C catalyst after the ADT was slightly decreased by 5–6% compared to that before the ADT, as a result of Cu dissolution during the electrochemical dealloying process (Fig. S6a–d in the Supplementary information). However, based on qualitative observations, the porous surface morphology and particle size of PtCu<sub>7</sub>@Pt catalyst did not significantly change during the ADT as shown in Fig. S6a and b of the Supplementary information.

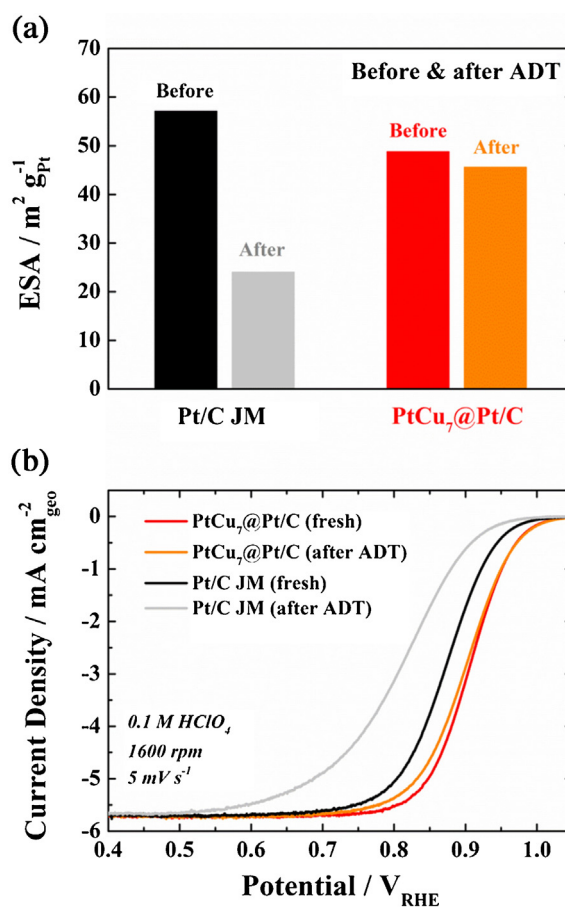
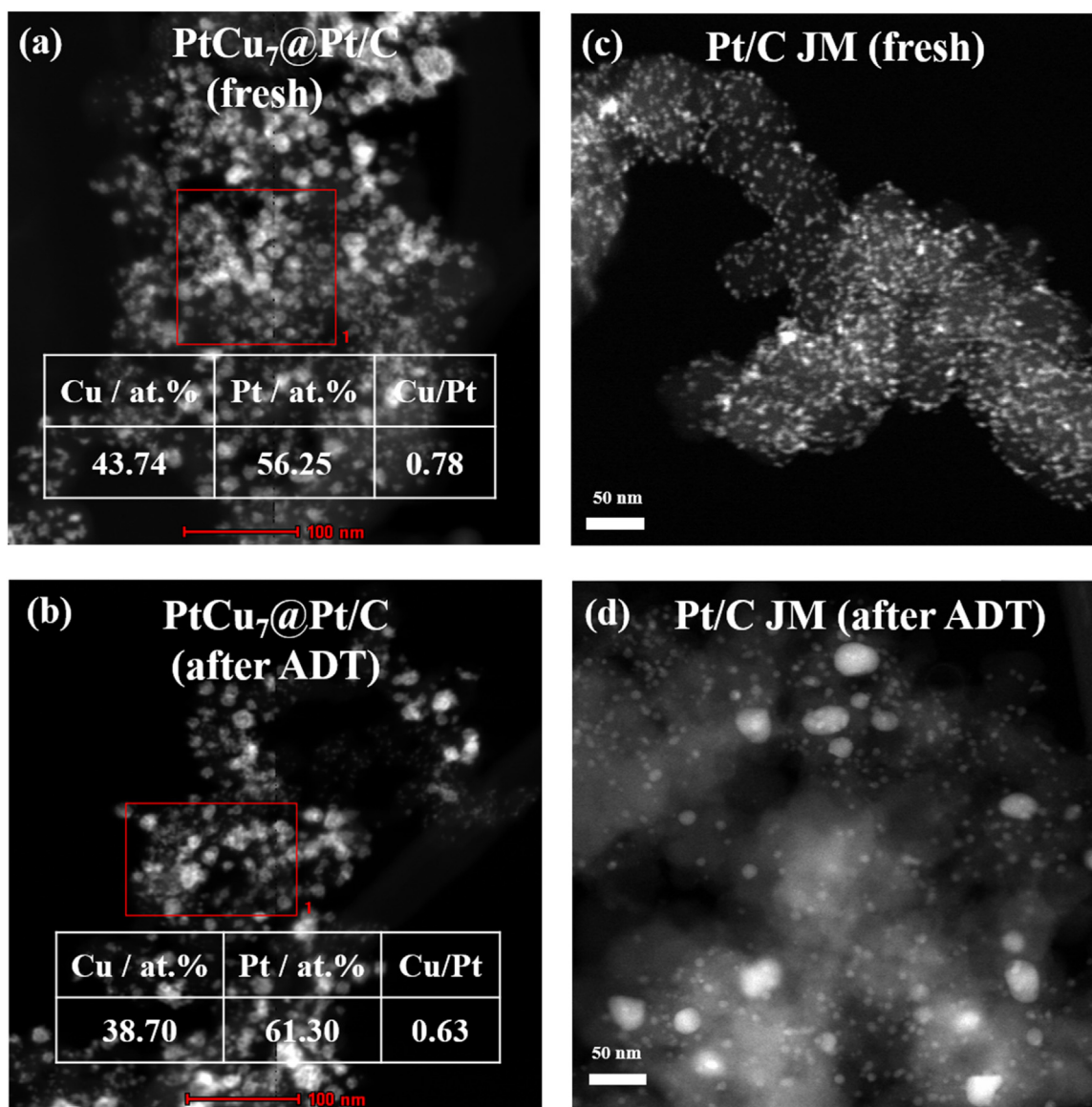


Fig. 7. (a) ESAs and (b) ORR polarization curves of Pt/C JM and PtCu<sub>7</sub>@Pt/C catalysts before and after the ADT.

The high durability of the PtCu<sub>7</sub>@Pt/C catalyst may be attributed to the increase in the dissolution potential of the Pt surface layers on the Cu-enriched subsurface layer. At the surface alloy, the dissolution potential shift of a 'solute' is closely related with the change in its surface segregation energy on a substrate (host) material. In case of the surface alloy composed of Cu (host) and Pt (solute), Pt atoms have a tendency to be segregated to the surface and to be stabilized because the surface segregation energy of Pt atoms becomes more negative (0.00 eV → -0.25 eV) on the Cu substrate [33]. Accordingly, the dissolution potential of Pt is positively shifted as much as ~0.25 V due to the stabilization of Pt atoms (standard dissolution potential of pure Pt = 1.18 V).

In addition, the Pt surfaces on PtCu<sub>7</sub>@Pt nanoparticles have a porous, but very solid structure, as a result of the surface compressive strain, which is generally observed in dealloyed PtM alloy nanoparticles [13,34]. Therefore, Cu dissolution from the subsurface regions of the nanoparticles was also considerably retarded, owing to the surface protection offered by stable Pt shell layers such as the case of Pt-skin structures [10,11].

On the other hand, in the case of the Pt/C JM catalyst, as shown in Fig. 8c and d, the Pt nanoparticles agglomerated to form very large particles after the ADT (Fig. S6e and f in the Supplementary information). Therefore, the degradation in the ORR activity of the Pt/C JM catalyst was mainly attributed to a decrease in the ESA as a result of ripening, agglomeration, and dissolution/redeposition of Pt nanoparticles [35]. Consequently, PtCu<sub>7</sub>@Pt/C was able to maintain its high ORR activity after the ADT, owing to the stable surface Pt structure, whereas the Pt/C JM catalyst suffered from



**Fig. 8.** STEM images and EDX results of PtCu<sub>7</sub>@Pt/C catalyst (a) before and (b) after the ADT. The Cu/Pt ratios were determined from the EDX spectra of the particles measured in red box regions of the STEM images. STEM images of Pt/C JM catalyst (c) before and (d) after the ADT. (For interpretation of the references to colour in this figure legend, the reader is referred to the web version of this article.)

severe structural changes such as particle agglomeration and was therefore, catalytically degraded.

#### 4. Conclusions

PtCu<sub>x</sub>@Pt/C core-shell catalysts with a porous surface structure were fabricated via the galvanic replacement reaction. The surface morphologies and compositions of the PtCu<sub>x</sub>@Pt/C catalysts were considerably influenced by the Cu to Pt ratios in the PtCu<sub>x</sub> nanoparticle substrates. Porous surfaces were produced on the PtCu<sub>x</sub>@Pt nanoparticles when the Cu to Pt ratios in the PtCu<sub>x</sub> nanoparticles were greater than 5. In addition, PtCu<sub>x</sub>@Pt nanoparticles with different nominal *x* values showed different electronic structures depending on the ratio of the surface to bulk compositions. The electronic structures and ORR activities of the PtCu<sub>x</sub>@Pt catalysts significantly changed as a function of the composition of Cu and Pt in the subsurface layers of the nanoparticles. Among the PtCu<sub>x</sub>@Pt catalysts, PtCu<sub>7</sub>@Pt/C exhibited superior ORR activity and durability compared to the commercially available Pt/C JM cat-

alyst. We believe that the synthesis strategy to make nano-sized pores on metal nanoparticle surfaces will provide new insights into the structural tuning of various energy nanomaterials.

#### Acknowledgements

This work was supported by the New & Renewable Energy Core Technology Program of KETEP grant funded by MOTIE, Korea (20133030011320, 20143030031340). This work was also supported by NRF grant funded by the Korea government (MSIP) (No. 2014R1A2A2A04003865, 2015R1C1A1A01053367, 2015R1A2A2A01007622).

#### Appendix A. Supplementary data

Supplementary data associated with this article can be found, in the online version, at <http://dx.doi.org/10.1016/j.apcatb.2016.05.028>.

## References

- [1] I.E.L. Stephens, A.S. Bondarenko, F.J. Perez-Alonso, F. Calle-Vallejo, L. Bech, T.P. Johansson, A.K. Jepsen, R. Frydendal, B.P. Knudsen, J. Rossmeisl, I. Chorkendorff, *J. Am. Chem. Soc.* 133 (2011) 5485–5491.
- [2] C. Wang, M. Chi, D. Li, D. Vliet, G. Wang, Q. Lin, J.F. Mitchell, K.L. More, N.M. Markovic, V.R. Stamenkovic, *ACS Catal.* 1 (2011) 1355–1359.
- [3] S.-Y. Huang, P. Ganesan, B.N. Popov, *ACS Catal.* 2 (2012) 825–831.
- [4] S.J. Hwang, S.-K. Kim, J.-G. Lee, S.-C. Lee, J.H. Jang, P. Kim, T.-H. Lim, Y.-E. Sung, S.J. Yoo, *J. Am. Chem. Soc.* 134 (2012) 19508–19511.
- [5] D. Wang, H.L. Xin, H. Wang, Y. Yu, E. Rus, D.A. Muller, F.J. DiSalvo, H.D. Abruña, *Chem. Mater.* 24 (2012) 2274–2281.
- [6] J. Yang, X. Chen, X. Yang, J.Y. Ying, *Energy Environ. Sci.* 5 (2012) 8976–8981.
- [7] Y. Lim, S.K. Kim, S.-C. Lee, J. Choi, K.S. Nahm, S.J. Yoo, P. Kim, *Nanoscale* 6 (2014) 4038–4042.
- [8] K.A. Kuttyiyel, K. Sasaki, Y.M. Choi, D. Su, P. Liu, R.R. Adzic, *Energy Environ. Sci.* 5 (2012) 5297–5304.
- [9] V.R. Stamenkovic, B.S. Mun, M. Arenz, K.J.J. Mayrhofer, C.A. Lucas, G. Wang, P.N. Ross, N.M. Markovic, *Nature Mater.* 6 (2007) 241–247.
- [10] C. Wang, M. Chi, D. Li, D. Strmcnik, D. Vliet, G. Wang, V. Komanicky, K.-C. Chang, A.P. Paulikas, D. Tripkovic, J. Pearson, K.L. More, N.M. Markovic, V.R. Stamenkovic, *J. Am. Chem. Soc.* 133 (2011) 14396–14403.
- [11] N. Jung, Y.-H. Chung, D.Y. Chung, K.-H. Choi, H.-Y. Park, J. Ryu, S.-Y. Lee, M. Kim, Y.-E. Sung, S.J. Yoo, *Phys. Chem. Chem. Phys.* 15 (2013) 17079–17083.
- [12] J. Durst, M. Lopez-Haro, L. Dubau, M. Chatenet, Y. Soldo-Oliver, L. Guetaz, P. Bayle-Guillemaud, F. Maillard, *J. Phys. Chem. Lett.* 5 (2014) 434–439.
- [13] P. Strasser, S. Koh, T. Anniyev, J. Greeley, K. More, C. Yu, Z. Liu, S. Kaya, D. Nordlund, H. Ogasawara, M.F. Toney, A. Nilsson, *Nature Chem.* 2 (2010) 454–460.
- [14] L. Gan, M. Heggen, S. Rudi, P. Strasser, *Nano Lett.* 12 (2012) 5423–5430.
- [15] J.A. Wittkopf, J. Zheng, Y. Yan, *ACS Catal.* 4 (2014) 3145–3151.
- [16] C.-M. Zhu, A. Gao, Y. Wang, Y. Liu, *Chem. Commun.* 50 (2014) 13889–13892.
- [17] M. Oezaslan, M. Heggen, P. Strasser, *J. Am. Chem. Soc.* 134 (2012) 514–524.
- [18] C. Xu, Y. Liu, J. Wang, H. Geng, H. Qiu, *ACS Appl. Mater. Interfaces* 3 (2011) 4626–4632.
- [19] M. Mohl, D. Dobo, A. Kukovec, Z. Konya, K. Kordas, J. Wei, R. Vajtai, P.M. Ajayan, *J. Phys. Chem. C* 115 (2011) 9403–9409.
- [20] M. Mohl, A. Kumar, A.L.M. Reddy, A. Kukovec, Z. Konya, I. Kiricsi, P.M. Ajayan, *J. Phys. Chem. C* 114 (2010) 389–393.
- [21] S.M. Alia, S. Pylypenko, K.C. Neyerlin, D.A. Cullen, S.S. Kocha, B.S. Pivovar, *ACS Catal.* 4 (2014) 2680–2686.
- [22] Y.-H. Chung, D.Y. Chung, N. Jung, H.Y. Park, S.J. Yoo, J.H. Jang, Y.-E. Sung, *J. Phys. Chem. C* 118 (2014) 9939–9945.
- [23] M. Schurmans, J. Luyten, C. Creemers, R. Declerck, M. Waroquier, *Phys. Rev. B* 76 (2007) 174208.
- [24] P. Mani, R. Srivastava, P. Strasser, *J. Phys. Chem. C* 112 (2008) 2770–2778.
- [25] R. Srivastava, P. Mani, P. Strasser, *J. Power Sources* 190 (2009) 40–47.
- [26] P. Strasser, S. Koh, J. Greeley, *Phys. Chem. Chem. Phys.* 10 (2008) 3670–3683.
- [27] D. Wang, Y. Yu, H.L. Xin, R. Hovden, P. Ercius, J.A. Mundy, H. Chen, J.H. Richard, D.A. Muller, F.J. DiSalvo, H.D. Abruña, *Nano Lett.* 12 (2012) 5230–5238.
- [28] M. Mohl, A. Kumar, A.L.M. Reddy, A. Kukovec, Z. Konya, I. Kiricsi, R. Vajtai, P.M. Ajayan, *J. Phys. Chem. C* 114 (2010) 389–393.
- [29] X. Lu, H.-Y. Tuan, J. Chen, Z.-Y. Li, B.A. Korgel, Y. Xia, *J. Am. Chem. Soc.* 129 (2007) 1733–1742.
- [30] T. Bligaard, J.K. Nørskov, *Electrochim. Acta* 52 (2007) 5512–5516.
- [31] A. Ruban, B. Hammer, P. Stoltze, H.L. Skriver, J.K. Nørskov, *J. Mol. Catal. A* 115 (1997) 421–429.
- [32] Y.-C. Tseng, H.-S. Chen, C.-W. Liu, T.-H. Yeh, K.-W. Wang, *J. Mater. Chem. A* 2 (2014) 4270–4275.
- [33] J. Greeley, J.K. Nørskov, *Electrochim. Acta* 52 (2007) 5829–5836.
- [34] R. Yang, J. Leisch, P. Strasser, M.F. Toney, *Chem. Mater.* 22 (2010) 4712–4720.
- [35] C.-H. Cui, H.-H. Li, S.-H. Yu, *Chem. Sci.* 2 (2011) 1611–1614.